Research Paper

A constitutive model for soil-rockfill mixtures

Andrea Brito[*], João Ribas Maranha, Laura Maria Mello Saraiva Caldeira

Geotechnical Department, Laboratório Nacional de Engenharia Civil (LNEC), Avenida do Brasil, n° 101, 1700-066 Lisbon, Portugal

ARTICLE INFO

ABSTRACT

Soil-rockfill mixtures (SRMs) are economical and environmentally friendly materials. Due to the absence in the literature of constitutive models specifically developed and tested for SRMs, a new constitutive model, the Subloading Surface Rockfill Model, is presented. This model allows the occurrence of plastic strains inside the yield surface, inducing a smooth elastic/plastic transition. The results of experimental tests for different coarse fractions (CF) of several SRMs performed on samples from Odelouca Dam are compared with those obtained with this model. The model was able to reproduce reasonably well the response of SRMs considering the intrinsic variability of the tested specimens.

1. Introduction

In the last decades, there has been a considerable increase in the use of soil-rockfill mixtures (SRMs) in embankments of high dams and other structures. It is an environmentally friendly material as it includes the excavation products from the spillways, cut-off trenches, outlet works and other appurtenant structures that would have to go to deposit and are instead reused. It is also an economic material since a significant part of it comes from near to the construction site, thereby reducing the costs of transportation.

In this work, the following definition of soil-rockfill mixtures is adopted [1]: (i) fraction retained on ¾″ (19 mm) sieve between 30% and 70%; (ii) fraction passing No. 200 (0.074 mm) sieve between 12% and 40%; (iii) and the maximum particle dimension (D_{max}) less than 2/3 of the embankment layer thickness after compaction and not larger than 0.40 m.

In this study, the coarse fraction, CF, is considered the fraction of the total sample retained on the ¾″ (19 mm) sieve and the finer fraction, FF, is consider the fraction of the total sample passing the same sieve (CF + FF = 1).

A literature review reveals the absence of constitutive models specifically developed for SRMs. Certainly this material presents a behaviour reflecting its two constituents – soil and rockfill. As such, the constitutive model that best reproduces its behaviour will have to take into account some important aspects of both materials. The main objective of this research was to developed a model, which should be as simple as possible but still capable of reproducing well the response of different SRMs subjected to undrained triaxial tests isotropically consolidated to multiple effective stresses and drained triaxial K_0 tests.

In the past SRMs were treated as a "weathered rockfill" or "transition material" and the constitutive models used for this type of material were those used for rockfill. The first models used in rockfill dams were linear elastic. According to some authors ([2–5]) this type of models presented good fitting to the observed results, which is not surprising considering that almost all these analyses were back analysis based on the monitoring results. However, soils present strain irreversibility even at relatively low stress states and the linear elastic models can only give a first approximation to the real mechanical behaviour.

The nonlinear elastic models were also very popular in the simulation of the mechanical behaviour of rockfill. The main objective of these models was to be able to fit the strain–stress curves of the tests. The bilinear model, the K-G model ([6] and [7]), the EC-K0 ([8]) model and the hyperbolic model are all examples of nonlinear elastic models.

In 1963, Konder [9] presented the hyperbolic model when he analysed strain–stress curves of soils subjected to conventional triaxial shear tests. He noted that these curves could be approximated by a hyperbolic function with a horizontal asymptote. Starting from this work, several authors proposed other hyperbolic models ([10–15], among others). Of these, Duncan and Chang model [10] has been the most used.

Examples of numerical analysis of three dams – Borde Seco Dam, Las Cuevas Dam and Alvito Dam, with the hyperbolic model can be found in [16].

A comparison between two different nonlinear elastic constitutive analytical models was presented by [17] for the predictions of the end of construction performance of a central core rockfill dam – Beliche Dam. The models used in these analyses were the K-G model and a modified version of the hyperbolic model of [10]. The hyperbolic model

---

* Corresponding author.

E-mail addresses: andreabrito@lnec.pt (A. Brito), jmaranha@lnec.pt (J.R. Maranha), laurac@lnec.pt (L.M.M.S. Caldeira).
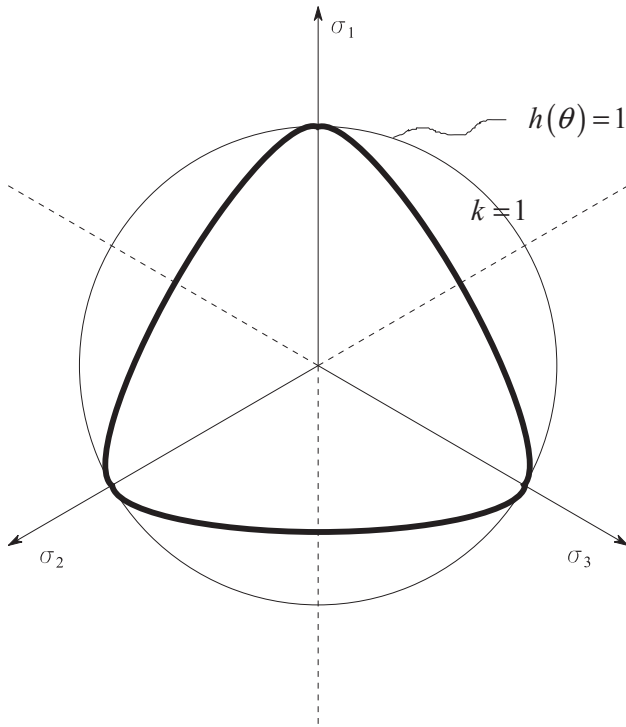
gave a less stiff response than the K-G model.

The failure of soils is not normally abrupt with a sudden reduction in stiffness. In fact, in most soils, large plastic deformations occur without complete loss of strength. It is even possible to stabilize failure in soil structures by removing the loading ([18]). Over the past 50 years, critical state models have been used to analyse and explain the behaviour of several materials ([19–26], among others).

The critical state model, known as Cam Clay, was initially developed for soils, in the 50s and 60s by researchers at the University of Cambridge ([19,27,20,28]). This model assumes that if the soil is subjected to an increasing shear strain, it will reach a critical state. A critical state model was also used to model Beliche Dam with a marked improvement over the non-linear elastic models [29].

However, the classic critical state models are hardening elastoplastic models and as such have some limitations. This paper presents a non-classic elastoplastic model, specifically developed for SRMs, that is capable of representing their main aspects of behaviour based on a large number of tests performed at LNEC on samples from Odelouca Dam, a large dam built with these materials. In the following section the model is described in detail. The model has also been used with considerable success in the numerical modelling of the construction of Odelouca Dam, which is described elsewhere [30].

In this analysis, the explicit finite difference program FLAC ([31]) was used. This is a two-dimensional program for geotechnical applications that allows the implementation of constitutive laws by the user.

In this work the usual soil mechanics convention that compressive stresses and strains are positive is adopted. Stresses are effective unless stated otherwise.

2. Subloading surface rockfill model

The Subloading Surface Concept ([32–34]) is a generalization of the conventional elastoplastic models that extends the elastoplasticity theory in such a way that the interior of the yield surface is not a purely elastic domain anymore, instead plastic strains are induced by the stress or strain rate inside the yield surface. So, the conventional yield surface is renamed as the normal yield surface. This concept was developed more deeply in [35] for rate dependent cyclic anisotropic structured behaviour.

In this formulation, differently from the original one by Hashiguchi [33], there is no restriction on the form of the yield surface. The yield function gradient is not normalized and the flow rule is non-associated.

The Subloading Surface Rockfill Model (SSRM) is an extension of the Modified Cam Clay Model (MCCM) with the Subloading Surface Concept, tensile strength, non-associated flow rule and a curved critical state line. Another difference is a non-circular deviatoric cross section, which implies dependence on the invariant θ. Geometrically, the yield surface is translated by ξp_c (constant that defines the effective tensile strength) in the negative direction of the hydrostatic axis. Despite, in principle, tensile strength not being present in SRMs, a very small value is useful to avoid some numerical problems such as singularity at the origin of stress space when computing the value of the scaling factor R and also for materials that present some tensile strength such as soils with structure.

A "continuous plasticity" formulation such as the subloading surface one was adopted partly because simpler hardening elastoplastic models, such as the Cam Clay model, were incapable of reproducing the observed inversion in the direction of the undrained triaxial effective stress paths. Complexities such as cyclic behaviour, rate dependency and anisotropy were also not considered as the model calibration for these aspects of behaviour was not evident from the tests performed. Several possible features of the model were investigated such as keeping an associated flow rule while changing the shape of the yield surface, hardening due to plastic shear strains and a volumetric strain dependent isotropic compression constant, λ^*, to represent particle breaking (clastic behaviour). As these particular features did not

Fig. 1. SSRM yield subloading, plastic potential surfaces and critical state line.

contribute to verifiable improvements in the model they were considered unnecessary complications and were not used in the final model.

The decreasing gradient of the critical state line is relevant for this type of material because the best fit for a straight CSL gives rise to a significant cohesion value. For the CSL to contain the origin of stress space, it follows that the greatest rate of change in the gradient occurs for small values of the mean effective stress making a curved CSL necessary. Non associativity was needed because the associative version of the model was incapable of reproducing simultaneously conventional triaxial compression and K_0 tests.

The yield surface used by the model, describes an ellipse in (p,q) space (as shown in Fig. 1), similar to the MCCM, and is represented by the following equation:

$$f(\boldsymbol{\sigma}) = \left(\frac{q}{M(\theta,p_c)}\right)^2 + \overline{p}\,(\overline{p} - p_c) = 0 \tag{1}$$

where $\overline{p} = p + \xi p_c$ and the invariants p, q and θ are defined in Appendix A.

The model requires at most ten material constants: λ^*, κ^*, ν, c_R, a, c, d, k, ξ and p_e. The constants λ^* and κ^* are determined so as to fit, respectively, to the slope of the normal compression line and the line of elastic unloading/reloading obtained under isotropic stress conditions in a bi-logarithmic representation ($\ln v - \ln p$), unlike the parameters λ, κ of the Cam Clay Model that are obtained in a semi-logarithmic representation ($v - \ln p$). The advantage of this approach is that the bulk modulus is independent of the specific volume, v, and is given by $K = \frac{p + p_e}{\kappa^*}$ while in the MCCM, the bulk modulus $K = \frac{vp}{\kappa}$ increases for looser states of the soil which is not in agreement with observed soil behaviour. The elastic law is isotropic nonlinear hypoelastic with the shear modulus given by $G = \frac{3(1-2\nu)}{2(1+\nu)}K$. The Poisson's ratio, ν, is constant. The material constant c_R is determined to adjust the evolution of stiffness with strain in the transition from elastic to elastoplastic behaviour. The constant ξ defines the effective tensile strength. p_e is a constant defined to make sure that the bulk modulus (K) is not zero even when the mean stress p is zero. The constant a defines the non-associativity degree with the associated model being recovered for $a = 1$. The constants c and d define the curved critical state in triaxial compression as

$$q = cp^d. \tag{2}$$

When $d = 1$, $c = M$ and $\xi = 0$ the straight critical state line is recovered. In general $d < 1$ as the critical state tangent friction angle decreases with the increase of p. The MCCM with the constants λ^* and κ^*, instead of the usual λ and κ, is obtained for a very large value of c_R, $a = 1$, $d = 1$, $\xi = 0$, $p_e = 0$ and $k = 1$. The constant k is given by

Fig. 2. Yield function cross section in the deviatoric plane.

$$k = \frac{M_e(p_c)}{M_c(p_c)} = \frac{\overline{M}_e(p_c)}{\overline{M}_c(p_c)}, \tag{3}$$

where M_c and M_e are the ratios of the longitudinal (triaxial) sections elipse semi-axes in compression and extension, $\overline{M}_c$ and $\overline{M}_e$ are the slopes of the secant Critical State Line (CSL) in triaxial compression and extension. The slope of the secant CSL is related to the ellipse semi-axes ratio by

$$\overline{M}(\theta, p_c) = \frac{M(\theta, p_c)}{1 - 2\xi} \tag{4}$$

The longitudinal ellipse semi-axes ratio, M, varies with θ and p_c according to $M(\theta, p_c) = M_c(p_c)h(\theta)$ and $M_c(p_c) = \frac{2c}{p_c}[(\frac{1}{2}-\xi)p_c]^d$ defines the flattening of the yield surface ellipse in triaxial compression. This results in a yield surface composed of elliptic sections with a rounded triangular shape as shown in Fig. 2. If $k = 1$ then $h(\theta) = 1$ and the trace of $f = 0$ on a deviatoric plane is a circle. $h(\theta)$ is given in Appendix A.

The subloading surface where the stress point must be at all times, is homothetic to the yield surface with scaling factor R. The image point in the yield surface $\sigma_y = \frac{1}{R}\sigma$ with $R \leqslant 1$. The subloading surface is defined as

$$\overline{f}(\sigma) = f(\sigma_y)|_{\sigma_y = \frac{1}{R}\sigma} = 0. \tag{5}$$

The value R, which is found by solving equation (5), is given in Appendix A. Fig. 3 represents the yield surface in 3D principal stress space together with the subloading surface.

The consistency condition, implying that the stress point must remain on the subloading surface during plastic loading, is given by

$$d\overline{f} = \frac{\partial \overline{f}}{\partial \sigma} : d\sigma + \frac{\partial \overline{f}}{\partial R}dR + \frac{\partial \overline{f}}{\partial p_c}dp_c = 0, \tag{6}$$

where

$$d\varepsilon^p = d\gamma \frac{\partial \overline{g}}{\partial \sigma} \tag{7}$$

is the non-associated flow rule,
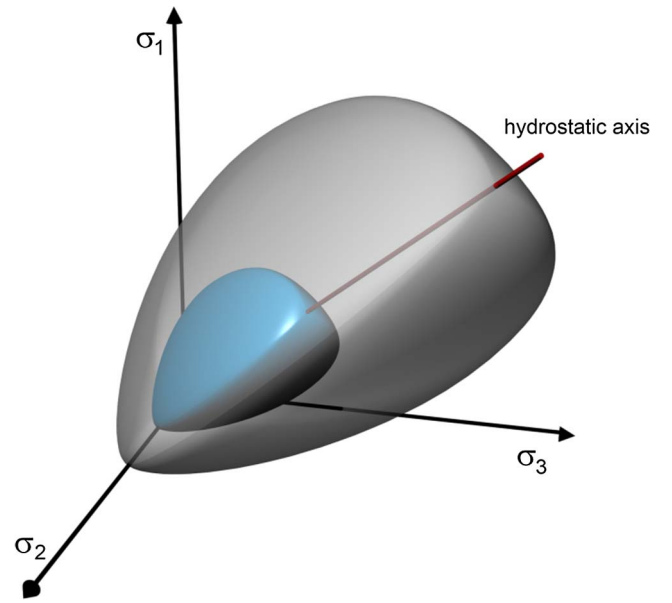
Fig. 3. SSRM yield and subloading surfaces in principal stress space.

$$d\sigma = \boldsymbol{D} : d\varepsilon^e = \boldsymbol{D} : (d\varepsilon - d\varepsilon^p) = K\mathrm{tr}(d\varepsilon^e)\boldsymbol{I} + 2G\mathrm{dev}(d\varepsilon^e) = \boldsymbol{D} : (d\varepsilon - d\gamma \frac{\partial \overline{g}}{\partial \sigma}) \tag{8}$$

is the elastic law. The plastic potential function is defined by

$$g(\sigma) = \left(\frac{q}{aM(\theta, p_c)}\right)^2 + \overline{p}(\overline{p} - p_c) = 0 \tag{9}$$

and the subloading plastic potential function is given by $\overline{g}(\sigma) = g(\sigma_y)|_{\sigma_y = \frac{1}{R}\sigma}$. Both are represented in Fig. 1.

The isotropic hardening law is given by:

$$dp_c = d\gamma l(\sigma, R, p_c) = (p_c + \frac{p_e}{1-\xi})\frac{1}{\lambda^* - \kappa^*}d\varepsilon_v^p \tag{10}$$

where

$$l(\sigma, R, p_c) = \left(p_c + \frac{p_e}{1-\xi}\right)\frac{1}{\lambda^* - \kappa^*}\mathrm{tr}\frac{\partial \overline{g}}{\partial \sigma} \tag{11}$$

and the subloading hardening law is described by

$$dR = U(R)\|d\varepsilon^p\| = d\gamma U(R)\left\|\frac{\partial \overline{g}}{\partial \sigma}\right\|. \tag{12}$$

$U(R)$ is a continuous function in $]0;+\infty[$ having the properties: $\lim_{R\to 0} U(R) = +\infty$, $\lim_{R\to +\infty} U(R) = -\infty$ and $U(1) = 0$. $U(R) = -c_R lnR$ is adopted for this model with the constant c_R defining the smoothness of the transition from elastic to elastoplastic behaviour. From the consistency condition the plastic multiplier, $d\gamma$, is determined as

$$d\gamma = \frac{\frac{\partial \overline{f}}{\partial \sigma} : \boldsymbol{D} : d\varepsilon}{\frac{\partial \overline{f}}{\partial \sigma} : \boldsymbol{D} : \frac{\partial \overline{g}}{\partial \sigma} + M_p}, \tag{13}$$

where the plastic modulus, M_p, is

$$M_p = -U(R)\left\|\frac{\partial \overline{g}}{\partial \sigma}\right\|\frac{\partial \overline{f}}{\partial R} - \frac{\partial \overline{f}}{\partial p_c}l(\sigma, R, p_c) \tag{14}$$

and

$$\frac{\partial \overline{f}}{\partial \sigma} : \boldsymbol{D} : \frac{\partial \overline{g}}{\partial \sigma} = K\mathrm{tr}\frac{\partial \overline{f}}{\partial \sigma}\mathrm{tr}\frac{\partial \overline{g}}{\partial \sigma} + 2G\mathrm{dev}\frac{\partial \overline{f}}{\partial \sigma} : \mathrm{dev}\frac{\partial \overline{g}}{\partial \sigma} \tag{15}$$

$$\boldsymbol{D} : \frac{\partial \overline{g}}{\partial \sigma} = \left(K - \frac{2}{3}G\right)\mathrm{tr}\frac{\partial \overline{g}}{\partial \sigma}\boldsymbol{I} + 2G\frac{\partial \overline{g}}{\partial \sigma}. \tag{16}$$
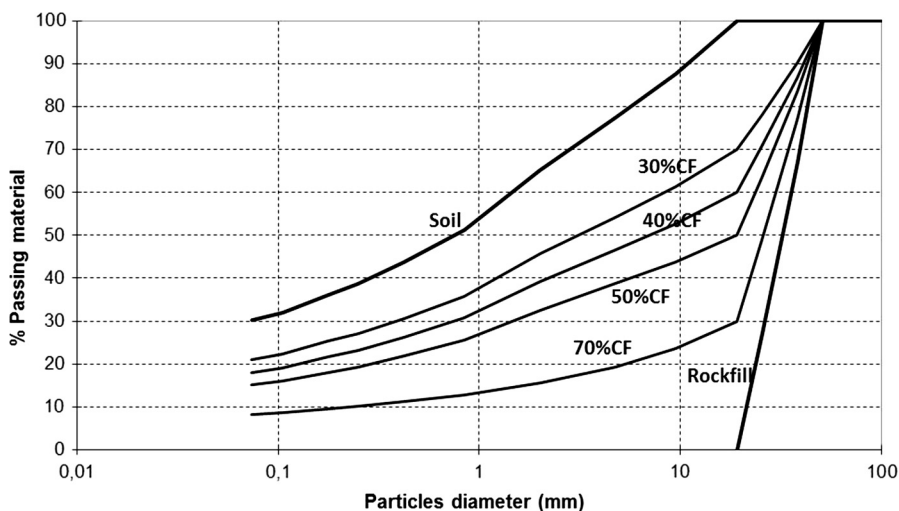
Fig. 4. Particle size distribution of the SRMs used.

The expressions for the gradients are presented in Appendix A.

The plastic loading condition under strain control is given by

$$\frac{\partial \overline{f}}{\partial \boldsymbol{\sigma}}: \boldsymbol{D}: d\boldsymbol{\varepsilon} = \frac{\partial \overline{f}}{\partial \boldsymbol{\sigma}}: d\boldsymbol{\sigma}^e = dp^e \mathrm{tr}\frac{\partial \overline{f}}{\partial \boldsymbol{\sigma}} + d\boldsymbol{s}^e: \mathrm{dev}\frac{\partial \overline{f}}{\partial \boldsymbol{\sigma}} > 0. \tag{17}$$

In contrast to conventional elastoplastic models it is possible for plastic loading to occur at any point inside the yield surface depending on the direction of loading, $d\varepsilon$, so the stress point is always on the subloading surface.

3. Modelling soil-rockfill mixtures with SSRM

The SSRM was implemented in the program *FLAC* in order to reproduce a set of tests on several samples: 30%CF, 40%CF, 50%CF and 70%CF. It was also applied to the pure soil and rockfill samples. The grain size distribution for all SRMs tested are presented in Fig. 4. According with the Unified Soil Classification System, the fines of the SRM used in the studies is classified as SM – silty sand with gravel. Both rockfill and soil result from weathered schist and greywacke obtained by quarrying. This material came from Odelouca Dam, which is an earth dam with 76 m height constructed in the south of Portugal using SRMs. Almost all the samples were constituted by three specimens of undrained triaxial compression tests consolidated isotropically to 200, 400 and 800 kPa of effective mean stress and a K0 consolidation test. The sample with 40%CF had another triaxial compression test consolidated isotropically to 1000 kPa and the soil sample included an additional specimen consolidated isotropically to 1600 kPa. The specimen dimensions used in the triaxial apparatus are about 230 mm in diameter and 450 mm in height. Each specimen is prepared by the vibrating compaction of about eight layers at the optimum point of standard Proctor test. More information about the experimental tests can be found in [30]. The experimental curves were chosen from a large number of SRM tests so that they were representative of average response.

A genetic algorithm (GA) was used in order to find out the model constants and initial values of variables that give the best fit to the laboratory test curves of the material. This type of algorithm is essential to determine the constants of complex constitutive models when multiple simultaneous experimental curves need to be fitted.

The genetic algorithms use concepts such as selection, inheritance and crossover in order to find a global optimal solution. In this algorithm an initial population is randomly generated, which is then used to simulate the tests using FLAC. After that, a fitness evaluation is carried out. A Hill Climbing procedure which is a local search optimisation technique that tries to improve the initial solution by changing its parameters is also performed. After, 25% of the best individuals are

selected, another 25% of new individuals are randomly generated, the remaining 50% of the individuals are generated by crossover and a new step is initialized with this new population. More details of this genetic algorithm can be found in [36].

A population with 128 individuals was used for all the samples modelled, the number of steps and the error for each sample are presented in Table 1. This error is obtained by a discrete version of Fréchet Distance [37]. This distance is a measure of similarity between curves that takes into account the location and ordering of the points along the curves. For each individual, the Discrete Fréchet Distance is computed between each experimental data curve and the corresponding model curve, and summed for all curve pairs. The main objective of the genetic algorithm is to minimise this distance.

Table 1 presents the number of curve pairs (test and model) that the algorithm had to compare at each step for each individual of the population in order to minimize the total error and also the average error *per* curve pair for each sample.

The model constants and initial values were assumed to be the same for each SRM CF value.

Despite always following the same preparation process which aims to obtain a sample having the maximum density from the Proctor test for a given SRM it is not possible to obtain perfectly uniform samples with precisely the same grading, particle composition, void ratio and water content, besides other aspects. Thus, the samples tested are assumed to be affected by a stochastic variation in properties that is implicitly considered when finding the set of material constants and initial values that best fits the measured response from different realizations of the same sample preparation process. In order to illustrate the material variability, the response of two 40%CF samples having almost the same void ratio is represented in Fig. 5. Contrary to what would be expected if the response were solely dependent on the void ratio, the marginally denser sample has lower strength and stiffness.

The samples that presented the larger error per curve pair were the

Table 1
Genetic algorithm data results.

Material	#steps	Error	#curve pairs	Error per curve pair
Soil	76	1.6444	10	0.16
30% *CF*	236	0.600	6	0.10
40% *CF*	118	1.695	10	0.17
50% *CF*	256	0.492	6	0.08
70% *CF*	79	1.545	8	0.19
70% *CF*[*]	143	0.863	6	0.14
Rockfill	260	0.744	6	0.12

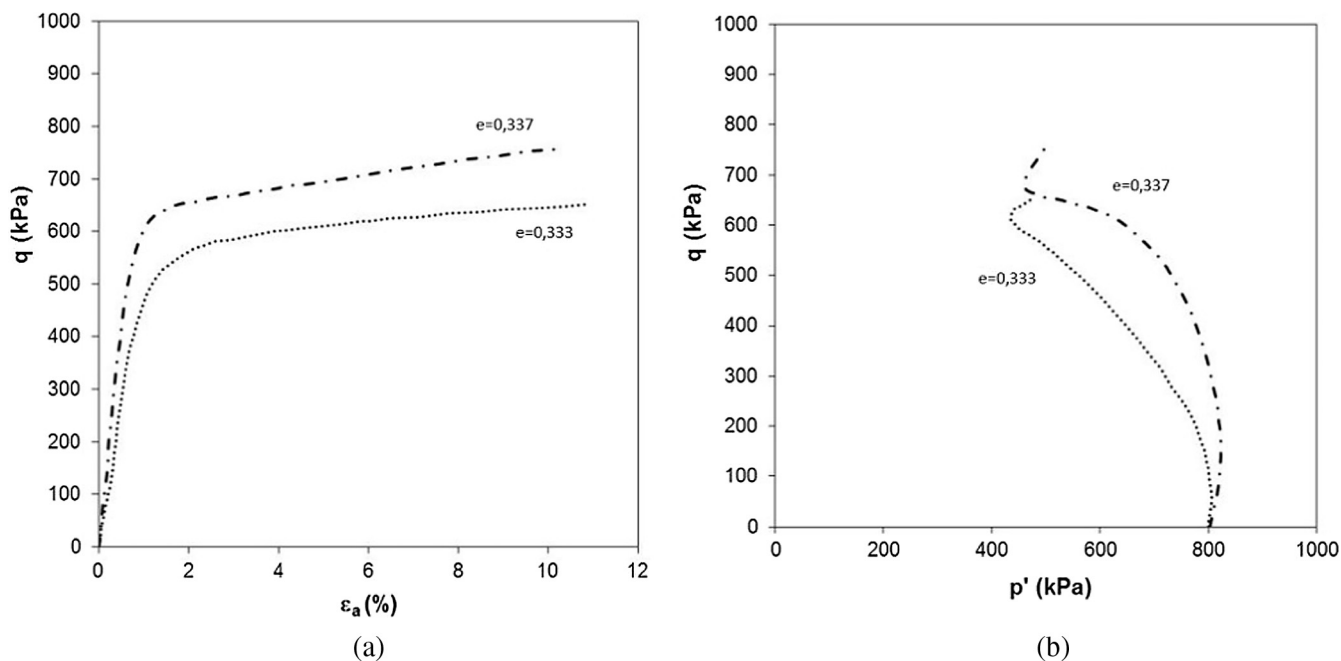[*] Sample constituted only with the three triaxial specimens.

Fig. 5. (a) deviatoric stress invariant *vs* axial strain and (b) effective stress paths from undrained triaxial tests isotropically consolidated to 800 kPa, for two 40%CF samples.

soils', the 40% CF and the 70% CF. However, these were also the samples with more curves to fit. Each one of the soil and 40% CF samples had eight curves for the triaxial tests and another two for the K_0 consolidation test. The 70% CF sample had six curves for the triaxial tests and another two for the K_0 consolidation test.

Because the SSRM induces plastic strains and hardening inside the yield surface, it is important to model the isotropic consolidation stage, where the initial values of the mean effective stress, p_0, and the yield stress, p_{c0}, have an important effect in the response of the model. As a result, they are also model parameters to be determined. p_0 represents the effective stress due to capillarity as the material is not saturated when compacted. p_{c0} represents the yield stress of the material due to the compaction procedure. They influence the subsequent behaviour of the material, and, as such, are expected to have a determinant effect on the stability and stress–strain response of the dam during construction.

The number of steps was quite variable and ranged between 76 (for the soil sample) and 260 (for the rockfill sample). The samples with fewer curve pairs needed more steps to converge to a solution. The smaller errors were obtained for the samples with a lower number of curves. This is to be expected as the model had to accommodate the specimen's variability. A large number of experimental curve pairs, each obtained from a different subsample of a larger given CF sample, can only be fitted in a least squares sense. Additionally, some tests can deviate more than others from the idealized conditions assumed when numerically modelling them. As an example, the samples are assumed to be in a homogeneous state of stress and strain. If this is clearly not the case the model might have difficulty in reproducing the results.

Table 2 shows the constants and initial values obtained for all the samples modelled. Some of these constants were fixed: $p_e = 1.0$ kPa, $\xi = 0.001$ (both to avoid numerical problems), $k = 0.71$ because all tests are in triaxial compression and as such the value does not influence the results and $\nu = 0.35$ for the soil and the SRM. Also the κ^* value used was the one found out from the isotropic compression tests. As such, the genetic algorithm only had to determine seven constants and two initial values except for the rockfill, where the value of the κ^* and the Poisson's ratio had also to be determined.

Figs. 4–11 show the comparison between the results from the undrained triaxial tests and the K_0 consolidation test and those computed with the SSRM, respectively, for the soil, 30% CF, 40%CF, 50% CF, 70% CF and rockfill samples. The figures show the deviatoric stress invariant *versus* the axial strain, and the effective stress paths.

By comparing the results, the constant a presented higher values for the soil sample and for the 40% CF and 70% CF samples. These samples are the ones which had also to adjust the results of the K_0 consolidation tests. Non associativity was introduced precisely because without it the model was incapable of reproducing both conventional triaxial compression and K_0 tests.

The sample that presented the best fitting, and so the lowest error per curve, was the 50% CF. This sample only had six curves to approximate and, as shown in Fig. 7, the three specimens had the same type of curve progress, showing that this was probably the SRM sample which presented less variability.

The worst fitting was obtained for the 70% CF sample with an error per curve of 0.19. The constants that better fit the experimental results
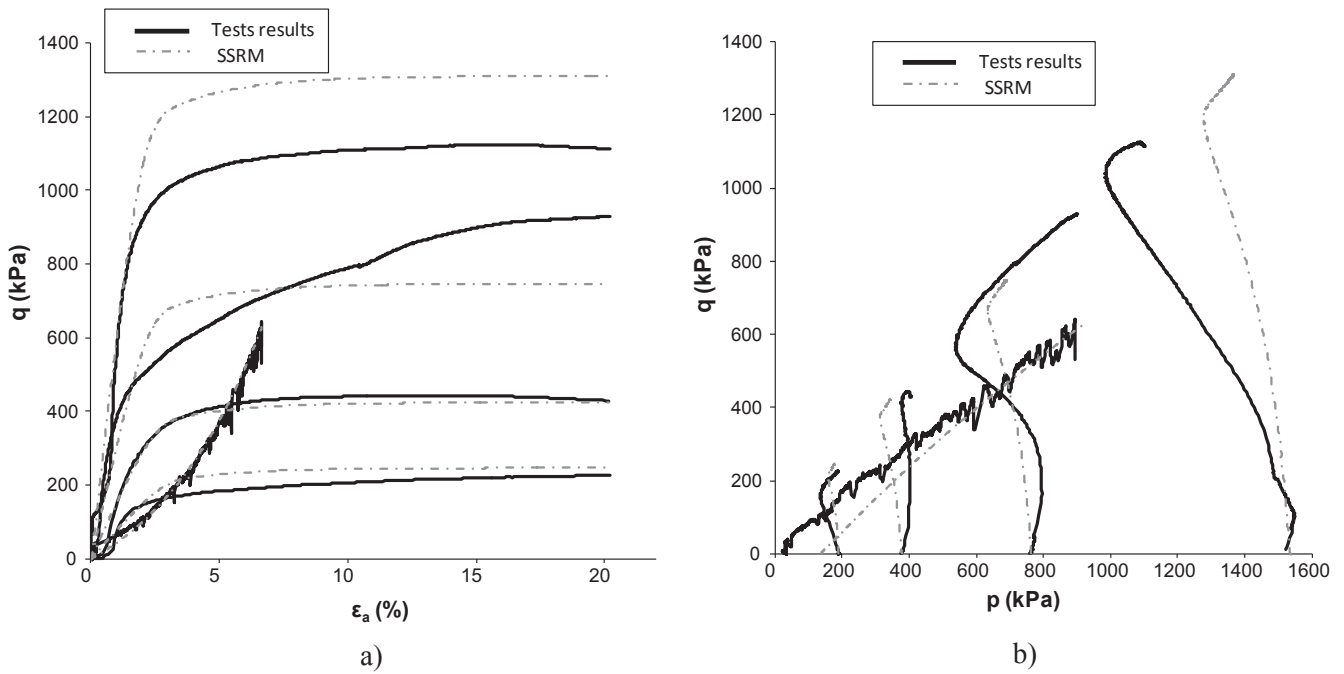
Table 2
Constants and initial values for the tested SRM using SSRM.

Material	ν	λ^*	κ^*	p_e (kPa)	c_R	a	ξ	c	d	p_0 (kPa)	p_{c0} (kPa)	k
Soil	0.35	0.0341	0.024	1.0	28.91	1.866	0.01	3.569	0.818	136.57	223.35	0.71
30% CF	0.35	0.070	0.006	1.0	12.37	0.503	0.01	4.554	0.808	138.98	399.56	0.71
40% CF	0.35	0.030	0.006	1.0	2.81	1.219	0.01	3.758	0.875	306.62	658.40	0.71
50% CF	0.35	0.047	0.002	1.0	11.71	0.317	0.01	5.420	0.806	16.65	199.34	0.71
70% CF	0.35	0.042	0.005	1.0	531.92	2.952	0.01	6.037	0.784	218.38	679.62	0.71
70% CF*	0.35	0.017	0.005	1.0	682.22	0.781	0.01	3.191	0.864	26.331	754.08	0.71
Rockfill	0.21	0.102	0.008	1.0	328.05	0.883	0.01	4.371	0.796	83.22	402.85	0.71

* Sample constituted only with the three triaxial specimens.

Fig. 6. Soil sample. Undrained triaxial tests with 190, 376, 760 and 1520 kPa isotropic consolidation, and the K_0 test representation for the experimental results and for *SSRM*: (a) deviatoric stress invariant *vs* axial strain and (b) effective stress paths.

cause a sudden transition between elastic and plastic behaviour with the highest value of c_R. This was possibly the sample with the most variability between subsamples. Variability of response in SRM samples can be significant as can be inferred from the large number of test results presented in [30].

In an attempt to improve the results for the 70% CF sample, a new analysis was performed considering only the three triaxial tests specimens. The results obtained are presented in Fig. 12.

Tables 1 and 2 also present the results for the 70% CF sample considering only the triaxial results. As can be seen, the results significantly improve from an error *per* curve pair of 0.19–0.14. Clearly,

the K_0 test curves were the most difficult to reproduce.

Table 3 presents a comparison between the values of the *c* and *d* constants of the equation (3) obtained directly from the triaxial tests assuming that a critical state was approximately attained in all the tests and fitting the final stress path points to a curve of the form $q_{cs} = cp_{cs}^d$ and those obtained with the genetic algorithm.

Some of the constants *c* and *d* that best fit all the curves for each sample obtained with the genetic algorithm were somewhat different from those obtained directly from the triaxial tests. This could, in part, be explained by the assumption used in directly computing the values from the tests, that a critical state was achieved or due to strain
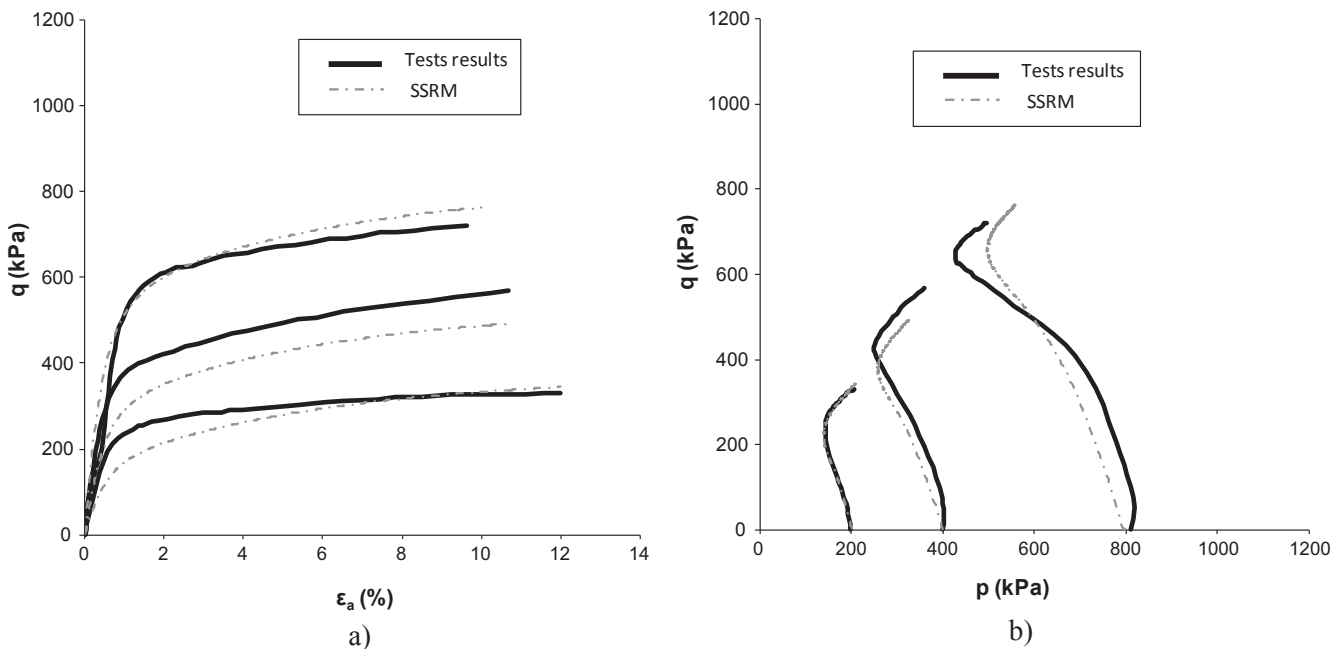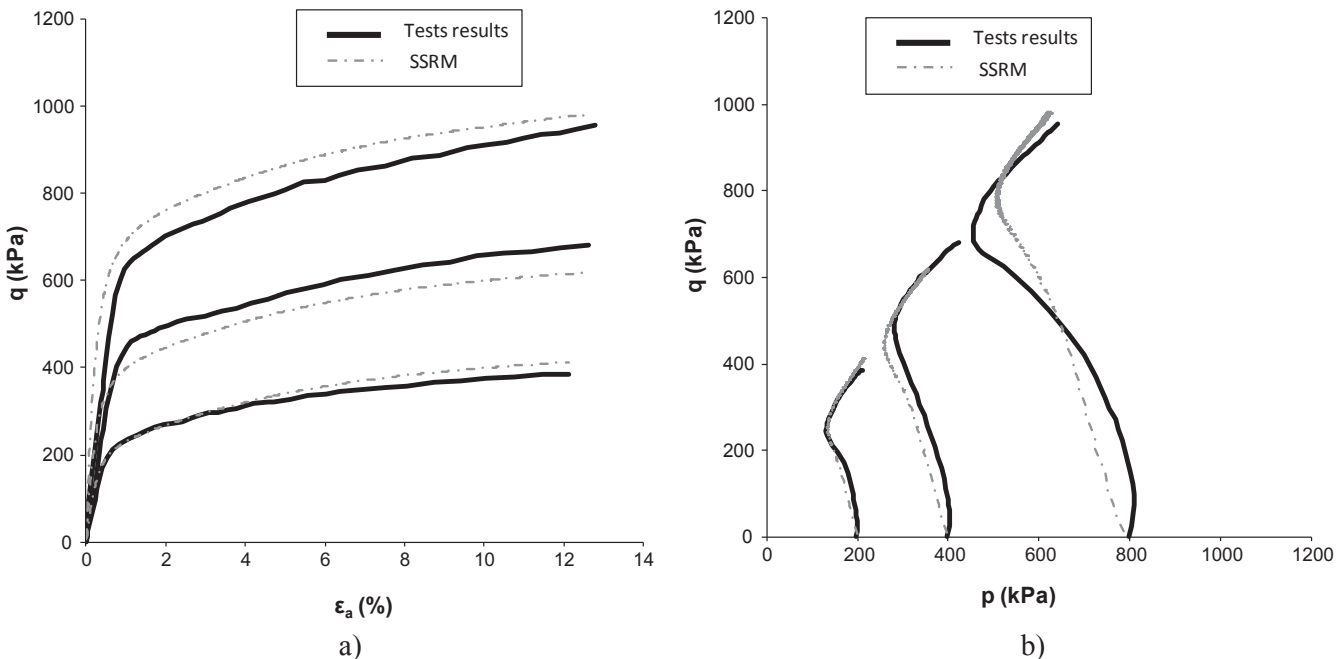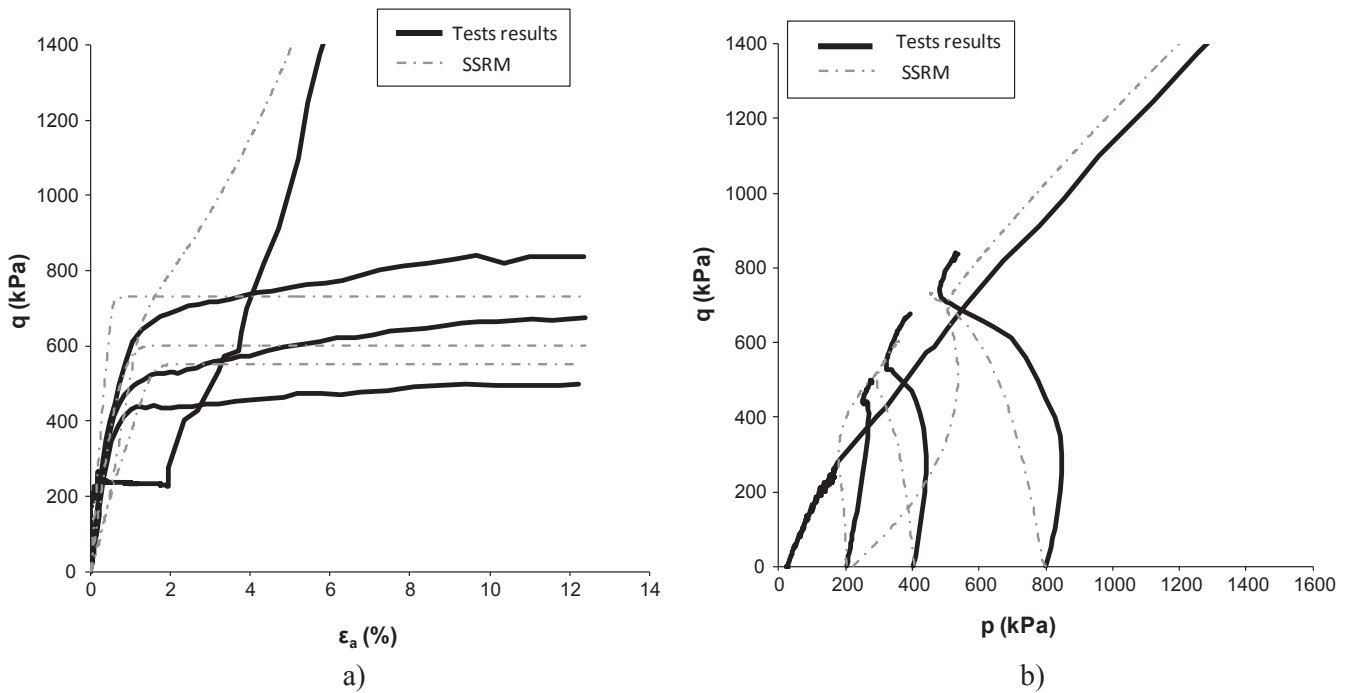

Fig. 7. 30% *CF* sample. Undrained triaxial tests with 200, 400 and 800 kPa isotropic consolidation representation for the experimental results and for *SSRM*: (a) deviatoric stress invariant *vs* axial strain and (b) effective stress paths.
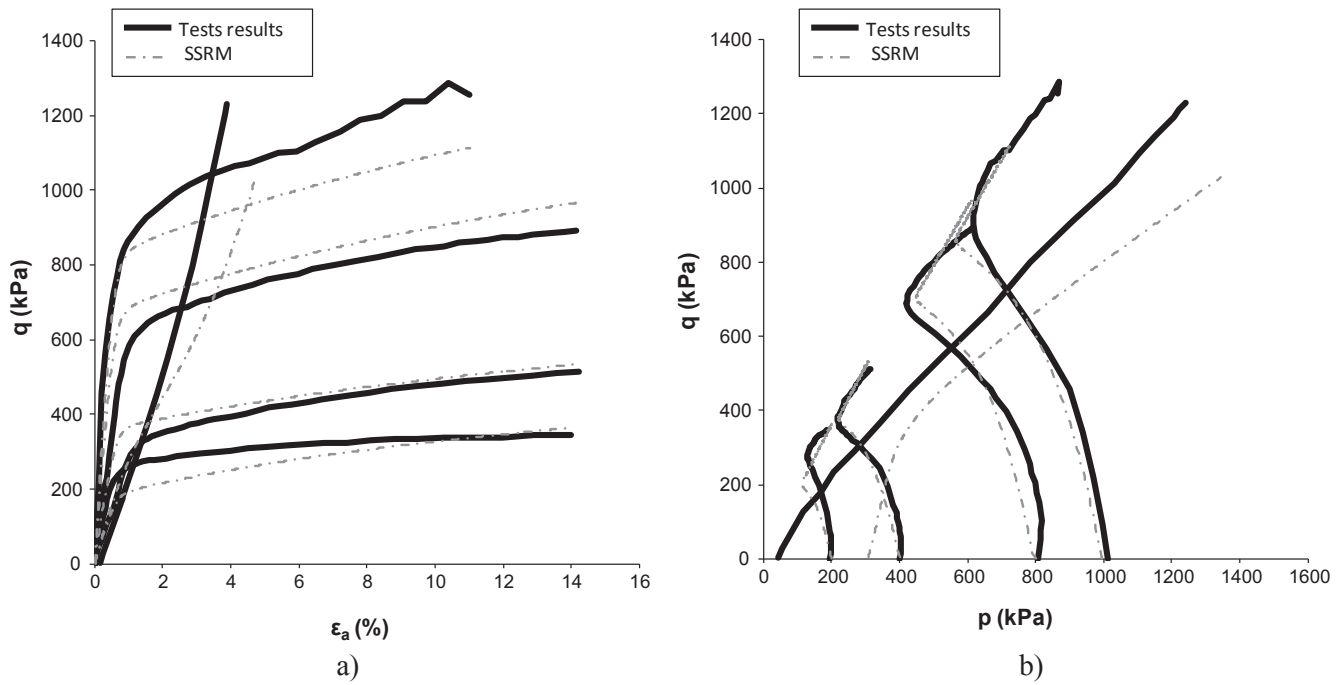
Fig. 8. 40%*CF* sample. Undrained triaxial tests with 200, 400, 800 and 1000 kPa isotropic consolidation, and the K_0 test representation for the experimental results and for *SSRM*: (a) deviatoric stress invariant *vs* axial strain and (b) effective stress paths.

localization. Also, this might occur with complicated constitutive models because it's often difficult to isolate the specific effect of a constant or to associate certain values to a specific mechanical and hydraulic material behaviour. For more sophisticated constitutive models, the constants and initial values usually are closely inter-connected and interfere with each other. This is why it is so important, when using complicated constitutive models, to use genetic algorithms or some similar tool in order to find out the best constants and initial values for each case.

It was also not possible to relate these constants and initial values obtained numerically with the coarse fraction present in the mixture.

This can happen because of multiple reasons. A possible one is the in-trinsic variability of the specimens. Another is that some of the samples had to approximate more curves and also different types of loading, such as triaxial and K_0 consolidation tests, while others only had to approximate triaxial tests.

Some simpler models were also used to try to represent the beha-viour of SRMs, such as MCCM but they represented the experimental SRMs curves very poorly. MCCM is an elastoplastic model and it ex-hibits a sharp transition in stiffness when going from elastic to elasto-plastic behaviour. This proved to be a limitation of the model for the SRMs since they show a more gradual transition. Also, the SRMs tested

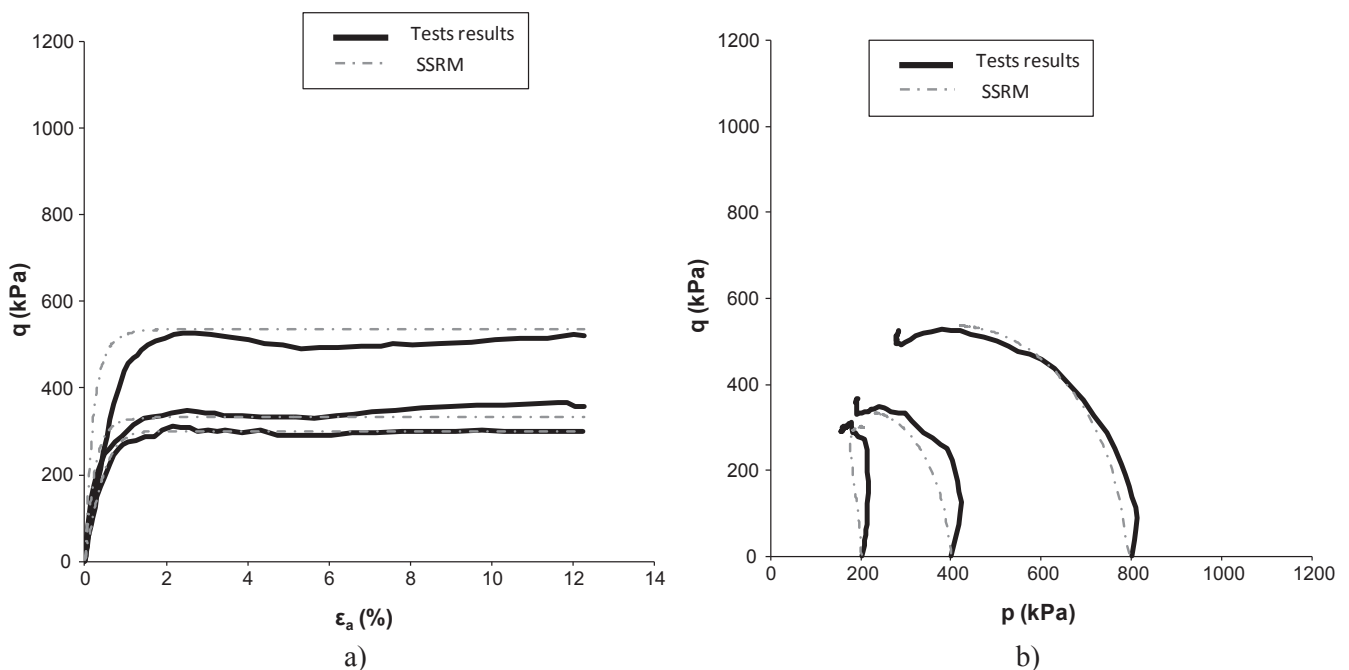**Fig. 9.** 50% *CF* sample. Undrained triaxial tests with 200, 400 and 800 kPa isotropic consolidation for the experimental results and for *SSRM*: (a) deviatoric stress invariant *vs* axial strain and (b) effective stress paths.
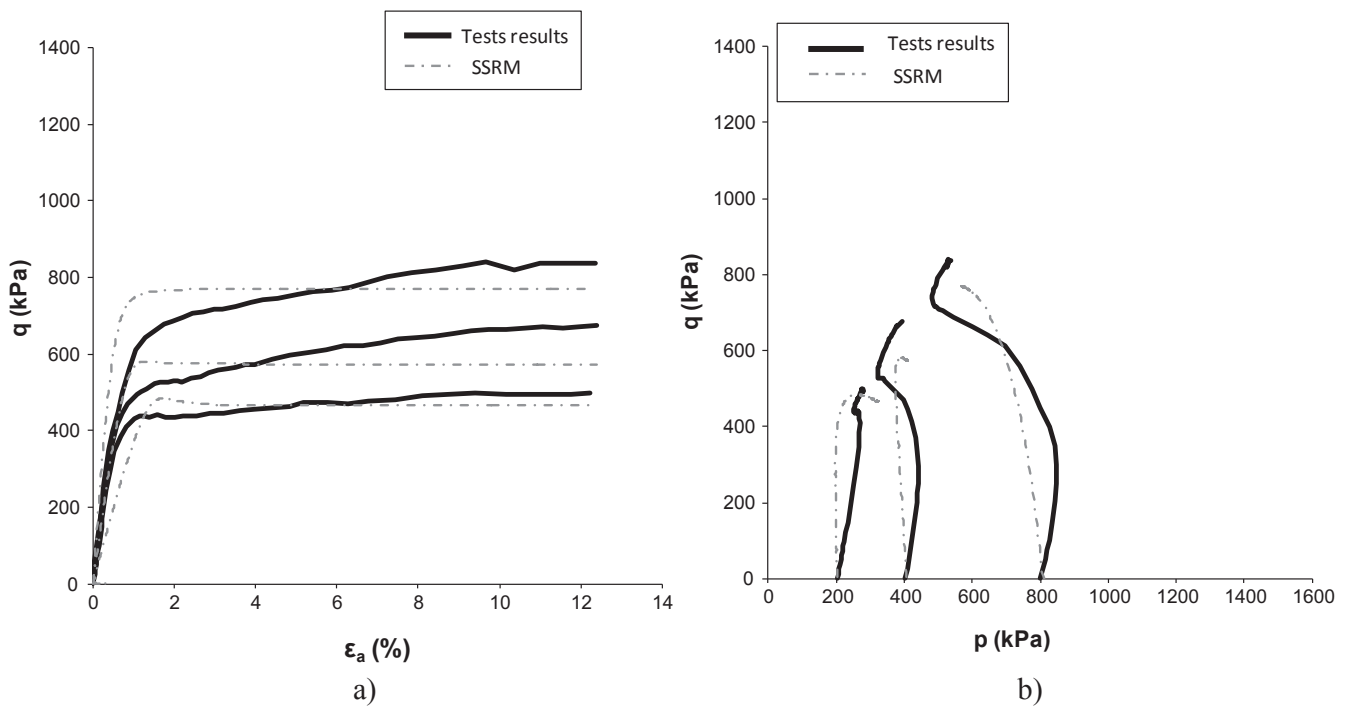
Fig. 10. 70% *CF* sample. Undrained triaxial tests with 200, 400 and 800 kPa isotropic consolidation, and the K_0 test representation for the experimental results and for *SSRM*: (a) deviatoric stress invariant *vs* axial strain and (b) effective stress paths.

presented an effective stress path with an inversion in direction which the MCCM was clearly unable to reproduce. The model was, as well, unable to reproduce the K_0 consolidation test. These results can be found in [30].

4. Conclusions

This paper presents a new model specifically developed for soil-rockfill mixtures, the Subloading Surface Rockfill Model (SSRM). This model is an extension of the MCCM with the Subloading Surface

Concept (which enables the occurrence of plastic strains inside the yield surface), tensile strength, non-associated flow rule and a curved critical state line. Another difference is a non-circular deviatoric cross section to account for reduced shear strength in triaxial extension. The tensile strength is useful to avoid some numerical problems and also for materials that present some actual tensile strength such as structured soils.

The model described was able to reproduce reasonably well the response of SRMs considering the intrinsic variability of the tested specimens and the number of experimental curves reproduced for each SRM. Some simpler models were used to try to represent the behaviour

Fig. 11. Rockfill sample. Undrained triaxial tests with 200, 400 and 800 kPa isotropic consolidation for the experimental results and for *SSRM*: (a) deviatoric stress invariant *vs* axial strain and (b) effective stress paths.

Fig. 12. 70% *CF* sample. Undrained triaxial tests with 200, 400 and 800 kPa isotropic consolidation for the experimental results and for *SSRM*: (a) deviatoric stress invariant *vs* axial strain and (b) effective stress paths.

Table 3
Comparison of the c and d constants obtained directly from tests and with the genetic algorithm.

Material	Directly from tests		Genetic Algorithm	
	c	d	c	d
Soil	1.904	0.908	3.569	0.818
30% *CF*	2.715	0.903	4.554	0.808
40% *CF*	4.355	0.833	3.758	0.875
50% *CF*	4.812	0.817	5.420	0.806
70% *CF*	6.315	0.779	6.037	0.784
70% *CF*[*]			3.191	0.864
Rockfill	2.256	0.966	4.371	0.796

* Sample constituted only with the three triaxial specimens.

of SRMs, such as MCCM but they represented the experimental SRMs curves very poorly. The experimental curves were chosen from a large number of SRM tests so that they were representative of average response. Also, the model constants and initial values were assumed to be the same for each SRM CF value.

In future developments, with additional experimental work, the model could be made easier to use if the possible dependency of the model's constants (and initial values of internal variables) on the void ratio were determined, but, as it is, the model is capable of reproducing well the irreversible volumetric strains, and as such the variation of the void ratio in drained conditions, as illustrated by the fitting of the undrained effective stress paths.

Appendix A. Appendix A

The invariants of the yield function defined as

$$p = \frac{1}{3}\text{tr }\boldsymbol{\sigma}, \tag{A.1}$$

$$q = \sqrt{\frac{3}{2}\boldsymbol{s}{:}\,\boldsymbol{s}} \tag{A.2}$$

with

$$\boldsymbol{s} = \text{dev }\boldsymbol{\sigma} \tag{A.3}$$

and the Lode's angle

$$\theta = \frac{1}{3}\sin^{-1}\left(\frac{27\det \boldsymbol{s}}{2q^3}\right) \tag{A.4}$$

In this work, the formulation of Willam and Warnke [38] is adopted, so $h(\theta)$ becomes

$$h(\theta) = \frac{2(1-k^2)\cos\left(\theta + \frac{\pi}{6}\right) + (2k-1)\sqrt{4(1-k^2)\cos^2\left(\theta + \frac{\pi}{6}\right) + 5k^2 - 4k}}{4(1-k^2)\cos^2\left(\theta + \frac{\pi}{6}\right) + (2k-1)^2}. \tag{A.5}$$

This describes an elliptic arc such that $h'(\pi/6) = h'(-\pi/6) = 0$, *i.e.* the curve has no corners (see Fig. 2). It depicts a smooth monotone transition between $h'(-\pi/6) = k$ and $h'(\pi/6) = 1$. The derivatives of the subloading surface and the subloading plastic potential function are given by

$$\frac{\partial \overline{f}}{\partial p_c} = \frac{2(1-d)}{p_c}\left(\frac{q}{RM(\theta, p_c)}\right)^2 + (2\xi - 1)\frac{p}{R} + 2\xi(\xi-1)p_c, \tag{A.6}$$

$$\frac{\partial \overline{f}}{\partial R} = -\frac{2}{R^2}\left(\frac{q}{M(\theta, p_c)}\right)^2 + p\left[\frac{p}{R} + \left(\xi - \frac{1}{2}\right)p_c\right]. \tag{A.7}$$

$$\frac{\partial \overline{g}}{\partial \boldsymbol{\sigma}} = \alpha \boldsymbol{I} + \beta \boldsymbol{s} + \gamma \boldsymbol{s}^2 \tag{A.8}$$

where

$$\alpha = \frac{1}{3R}\left[\frac{2p}{R} + (2\xi-1)p_c\right] + \frac{2h'(\theta)q}{(RaM(\theta, p_c))^2 h(\theta)\cos(3\theta)}, \tag{A.9}$$

$$\beta = \frac{3}{(RaM(\theta, p_c))^2}\left\{1 + \frac{h'(\theta)\sin(3\theta)}{h(\theta)\cos(3\theta)}\right\} \tag{A.10}$$

and

$$\gamma = \frac{9h'(\theta)}{(RaM(\theta, p_c))^2 h(\theta)q\cos(3\theta)}. \tag{A.11}$$

$\frac{\partial \overline{f}}{\partial \sigma}$ is obtained from the expression for $\frac{\partial \overline{g}}{\partial \sigma}$ with $a = 1$. The gradient of $\overline{g}(\sigma)$ at the triaxial compression plane is given by $\theta = \frac{\pi}{6}$, $h(\frac{\pi}{6}) = 1$ and $\lim_{\theta \to \frac{\pi}{6}}\frac{h'(\theta)}{\cos(3\theta)} = \frac{1-k^2}{(1-2k)^2}$, so that,

$$\alpha = \frac{1}{3R}\left[\frac{2p}{R} + (2\xi-1)p_c\right] + \frac{2q}{(RaM)^2(1-2k)^2}, \tag{A.12}$$

$$\beta = \frac{3}{(RaM)^2}\left\{1 + \frac{1-k^2}{(1-2k)^2}\right\} \tag{A.13}$$

and

$$\gamma = \frac{9(1-k^2)}{(RaM)^2 q(1-2k)^2}. \tag{A.14}$$

At the triaxial extension plane the gradient is given by $\theta = -\frac{\pi}{6}$, $h(-\frac{\pi}{6}) = k$ and $\lim_{\theta \to -\frac{\pi}{6}}\frac{h'(\theta)}{\cos(3\theta)} = \frac{2k(k^2-1)}{3(k-2)}$, so that,

$$\alpha = \frac{1}{3R}\left[\frac{2p}{R} + (2\xi-1)p_c\right] + \frac{4q(1-k^2)}{(RaM)^2 3(k-2)}, \tag{A.15}$$

$$\beta = \frac{3}{(RaM)^2}\left\{1 + \frac{2(1-k^2)}{3(k-2)}\right\} \tag{A.16}$$

and

$$\gamma = \frac{6(1-k^2)}{(RaM)^2 q(k-2)}. \tag{A.17}$$

The value of the subloading surface scaling factor R is given by

$$R = \frac{1}{2\xi(\xi-1)}\left\{(1-2\xi)p - \sqrt{(2\xi-1)^2 p^2 - 4\xi(\xi-1)\left[\left(\frac{q}{M(\theta, p_c)}\right)^2 + p^2\right]}\right\}, \tag{A.18}$$

which for $\xi = 0$ becomes

$$R = \frac{1}{pp_c}\left[\left(\frac{q}{M}\right)^2 + p^2\right] \tag{A.19}$$

In this case the value of R is not defined at $p = q = 0$ making a case of using a very small value of ξ even for materials with no tensile strength. Close to the hydrostatic axis it may be assumed that $h(\theta) = 1$ and $h'(\theta) = 0$, that is to say that h becomes independent of θ. So, $\frac{\partial \overline{f}}{\partial \sigma} = \alpha \boldsymbol{I}$ and

$$\alpha = \frac{1}{3R}\left[\frac{2p}{R} + (2\xi-1)p_c\right], \tag{A.20}$$

with $\beta = \gamma = 0$.

Considering $h(\theta) = \frac{u}{v}$, where

$$u = 2k_1\bar{c} + k_2\sqrt{4k_1\bar{c}^2 + k(5k-4)}, \tag{A.21}$$

$$v = 4k_1\bar{c}^2 + k_2^2, \tag{A.22}$$

$$k_1 = 1-k^2, \tag{A.23}$$

$$k_2 = 2k-1, \tag{A.24}$$

$$\bar{c} = \cos\left(\frac{\pi}{6} + \theta\right) \text{ and} \tag{A.25}$$

$$s = \sin\left(\frac{\pi}{6} + \theta\right), \tag{A.26}$$

So that,

$$\frac{dh(\theta)}{d\theta} = h'(\theta) = -\frac{2k_1 s}{v}\left\{1 + \bar{c}\left[\frac{2k_2^2}{u-2k_1\bar{c}} - 4h(\theta)\right]\right\} \tag{A.27}$$

References

[1] JAE/LNEC. Normas da Junta Autónoma de Estradas. JAE/LNEC, Lisboa; 1998.
[2] Penman A, Burland J, Charles J. Observed and predicted deformations in large embankment dams during construction. Proc Inst Civ Eng 1971;49:1–21.
[3] Penman A, Charles J. Construction deformations in a rockfill dam. In: Proceedings ASCE, Journal of the Soil Mechanics and Foundations Division, vol. SM2; 1973. p. 139–63.
[4] Mahler CF. A discussion to Professor Eisenstein's paper: the role of constitutive laws in analysis of embankments. In: Proceddings of the 3th ICNMG, Aachen; 1979.
[5] Cathie D, Dungar R. Evaluation of finite element predictions for construction behaviour of a rockfill dam. Proc Inst Civ Eng 1978;65(2):551–68.
[6] Nelson I, Baron M. Application of variable moduli models to soil behaviour. Int J Solids Struct 1971;7(Issue 4):399–417.
[7] Naylor DJ, Pande GN, Simpson B, Tabb R. Finite elements in geotechnical engineering, Swansea, U.K. (SW/75), 245: Pineridge Press Ltd.; 1981.
[8] Veiga Pinto A. Previsão do comportamento estrutural de barragens de enrocamento, Tese para obtenção do grau de especialista, LNEC, Lisboa; 1983.
[9] Konder RL. A hyperbolic stress-strain response: cohesive soils. J Soil Mech Found Divis, ASCE 1963;89(1):115–43.
[10] Duncan JM, Chang YC. Nonlinear analysis of stress and strain in soils. J Soil Mech Found Divis, ASCE 1970;96(SM5):1629–53.
[11] Kulhawy FH, Duncan JM, Seed HB. Finite element analysis of stresses and movements in embankments during construction, Rep. 569-8. U.S. Army Corps of Engineers Waterways Exp. Stn., Visksburg, Miss.; 1969.
[12] Kulhawy FH, Duncan JM. Stresses and movements in Oroville dam. J Soil Mech Found Divis 1972;98(SM7):653–65.
[13] Duncan JM. Hyperbolic stress-strain relationships. In: Proceedings of the workshop in limit equilibrium, plasticity and generalized stress-strain in geotechnical engineering; 1980.
[14] Habibagahi G, Mokhberi M. A hyperbolic model for volume change behaviour of collapsible soils. Can Geotech J 1998;35(2):264–72.
[15] Chen RP, Zhou WH, Cao WP, Chen YM. Improved hyperbolic model of load-transfer for pile-soil interface and its application in study of negative friction of single piles considering time effect. Yantu Goncheng Xuebao (Chin J Geotech Eng) 2007;29(6):824–30.
[16] Caldeira L. Comportamento dinâmico de barragens de aterro. PhD Thesis. Faculdade de Engenharia da Universidade do Porto, Porto; 1994.
[17] Naylor DJ, Maranha das Neves E, Mattar D, Veiga Pinto A. Prediction of construction performance of Beliche dam. Géotechnique 1986;36(3):359–76.
[18] Maranha das Neves E. Mecânica dos solos, Lisboa: Instituto Superior Técnico; 2002.
[19] Roscoe KH, Schofield AN, Wroth CP. On the yielding of soils. Géotechnique 1958;8:22–52.
[20] Schofield AN, Wroth CP. Critical state soil mechanics. London: McGraw-Hill; 1968.
[21] Carter JP, Booker JR, Wroth CP. A critical state soil model for cyclic loading. In: Pande GN, Zienkiewicz OC, editors. Soil mechanics - transient and cyclic loads, Wiley, New York; 1982. p. 219–52.
[22] Dafalias YF. Bounding surface plasticity I: mathematical foundation and hypoelasticity. J Eng Mech (ASCE) 1986;112(EM9):966–87.
[23] Britto AM, Gunn MJ. Critical state soil mechanics via finite elements. Chichester: Ellis Horwood; 1987.
[24] Gens A, Potts DM. Critical state models in computational geomechanics. Eng Comput 1988;5:178–97.
[25] Borja RI, Lee SR. Cam Clay plasticity. Part I: Implicit integration of elastoplastic constitutive relations. Comput Methods Appl Mech Eng 1990;78:49–72.
[26] Been FG, Jefferies MG. A state parameter for sands. Géotechnique 1985;35(2):127–32.
[27] Roscoe KH, Schofield AN. Mechanical behaviour of an idealised wet clay. In: Proceedings of the 2nd European conference on soil mechanics and foundation engineering, Wiesbaden; 1963.
[28] Roscoe KH, Burland JB. On the generalised stress-strain behaviour of "wet clay". In: Eng Plasticity, Cambridge Univ. Press, Cambridge; 1968. p. 535–609.
[29] Naylor DJ, Maranha JR, Maranha das Neves E, Veiga Pinto AA. A back-analysis of Beliche Dam. Géotechnique 47(2), 221–33.
[30] Brito A. Use of soil-rockfill mixtures in embankments dams PhD Thesis Lisboa: Instituto Superior Técnico, Universidade de Lisboa; 2015
[31] Itasca Software. Flac Manual, Minneapolis, Itasca; 2008.
[32] Hashiguchi K, Ueno M. Elastoplastic constitutive laws of granular materials. Constitutive Equations of Soils. In: Proc 9th Int conf soil mech found engng, Special Session 9, Tokyo; 1977.
[33] Hashiguchi K. Constitutive equations of elastoplastic materials with elastic-plastic transition. J Appl Mech ASME 1980;47(2):266–72.
[34] Hashiguchi K. Subloading surface model in unconventional plasticity. Int J Solids Struct 1989;25(8):917–45.
[35] Maranha J, Pereira C, Vieira A. A viscoplastic subloading soil model for rate-dependent cyclic anisotropic structured behaviour. Int J Numer Anal Meth Geomech; 2016. p. 1–25.
[36] Pereira C, Maranha J, Brito A. Advanced constitutive model calibration using genetic algorithms: some aspects. In: 8th European conference on numerical methods in geotechnical engineering; 2014.
[37] Fréchet M. Sur quelques points du calcul fonctionnel. In: Rendiconto de Circolo Mathematico di Palermo Palermo, 1906;22:1–74.
[38] Willam KJ, Warnke EP. Constitutive model for the triaxial behaviour of concrete. In: International association for bridge and structure engineering proceedings, vol. 19, Bergamo, Italy; 1975.